STARD3 or STARD3NL and VAP form a novel molecular tether between late endosomes and the ER

Fabien Alpy[1,2,3,4,*], Adrien Rousseau[1,2,3,4], Yannick Schwab[2,4,5,‡], François Legueux[1,2,3,4], Isabelle Stoll[1,2,3,4], Corinne Wendling[1,2,3,4], Coralie Spiegelhalter[2,3,4,5], Pascal Kessler[2,3,4,5], Carole Mathelin[4,6], Marie-Christine Rio[1,2,3,4], Timothy P. Levine[7] and Catherine Tomasetto[1,2,3,4]

[1]Institut de Génétique et de Biologie Moléculaire et Cellulaire (IGBMC), Functional Genomics and Cancer Department, 1 rue Laurent Fries, Illkirch, 67404, France
[2]Institut National de la Santé et de la Recherche Médicale (INSERM), U 964, Illkirch, France
[3]Centre National de la Recherche Scientifique (CNRS), UMR 7104, Illkirch, France
[4]Université de Strasbourg, Illkirch, France
[5]IGBMC, Imaging center, Illkirch, France
[6]CHU de Strasbourg, Département de Sénologie, Hôpital de Hautepierre, Strasbourg, France
[7]Division of Cell Biology, University College London Institute of Ophthalmology, London, UK
[‡]Present address: EMBL, 69117 Heidelberg, Germany
*Author for correspondence (Fabien.Alpy@igbmc.fr)

Accepted 24 September 2013
Journal of Cell Science 126, 5500–5512

doi: 10.1242/jcs.139295

Summary

Inter-organelle membrane contacts sites (MCSs) are specific subcellular regions favoring the exchange of metabolites and information. We investigated the potential role of the late-endosomal membrane-anchored proteins StAR related lipid transfer domain-3 (STARD3) and STARD3 N-terminal like (STARD3NL) in the formation of MCSs involving late-endosomes (LEs). We demonstrate that both STARD3 and STARD3NL create MCSs between LEs and the endoplasmic reticulum (ER). STARD3 and STARD3NL use a conserved two phenylalanines in an acidic tract (FFAT)-motif to interact with ER-anchored VAP proteins. Together, they form an LE–ER tethering complex allowing heterologous membrane apposition. This LE–ER tethering complex affects organelle dynamics by altering the formation of endosomal tubules. An *in situ* proximity ligation assay between STARD3, STARD3NL and VAP proteins identified endogenous LE–ER MCS. Thus, we report here the identification of proteins involved in inter-organellar interaction.

Key words: Endoplasmic reticulum, Endosome, Membrane contact site, MLN64, MENTHO, START domain, MENTAL domain

Introduction

Eukaryotic cells are composed of multiple membrane-bound organelles that define environments dedicated to specific metabolic activities. This organization implies the necessity for inter-organelle exchange of metabolites and information. In addition to membrane-bound carriers, organelles can exchange substances through areas where heterologous membranes from two distinct organelles come into close apposition; these areas are termed membrane contact sites (MCSs) (Levine and Loewen, 2006). In most eukaryotic cells MCSs have been observed between the endoplasmic reticulum (ER) and multiple distinct organelles, including the plasma membrane, mitochondria and Golgi apparatus (Elbaz and Schuldiner, 2011; Toulmay and Prinz, 2011). One of the most studied MCSs involves the ER and mitochondria; these MCSs appear essential for transfer of small molecules such as calcium or lipids, between the two organelles (Elbaz and Schuldiner, 2011). At an MCS, the close apposition between membranes (~10–20 nm) requires specific tethers involving protein–protein or protein–lipid interactions (Levine and Loewen, 2006). For instance, in mammalian cells, the ER and mitochondria are tethered in part by homotypic bridges formed by mitofusin 2, which is found on the outer membrane of both the mitochondria and the ER (de Brito and Scorrano, 2008). However to date, most organelle tethering complexes remain to be determined.

Potential components of MCS bridging complexes should possess a membrane anchoring domain mediating its attachment to one organelle and an additional domain projecting into the cytoplasm that is able to recruit components of another organelle. The STARD3 [StAR (steroidogenic acute regulatory protein) related lipid transfer (START) domain-3] and STARD3NL (STARD3 N-terminal like) proteins, are good candidates for components of MCS bridging complexes. Both STARD3, previously known as MLN64 (metastatic lymph node 64) (Alpy et al., 2001), and STARD3NL, previously known as MENTHO (Alpy et al., 2002), possess a conserved membrane-spanning domain with four transmembrane helices named MENTAL (MLN64 N-terminal) (Alpy et al., 2005), which targets these proteins to the limiting membranes of late endosomes (LEs; Fig. 1A) (Alpy et al., 2001; Alpy et al., 2002). In addition, the N- and C-terminal extremities of both STARD3 and STARDNL project into the cytosol (Fig. 1A) (Alpy et al., 2001; Alpy et al., 2002). STARD3 is longer than STARD3NL, possessing an

Journal of Cell Science

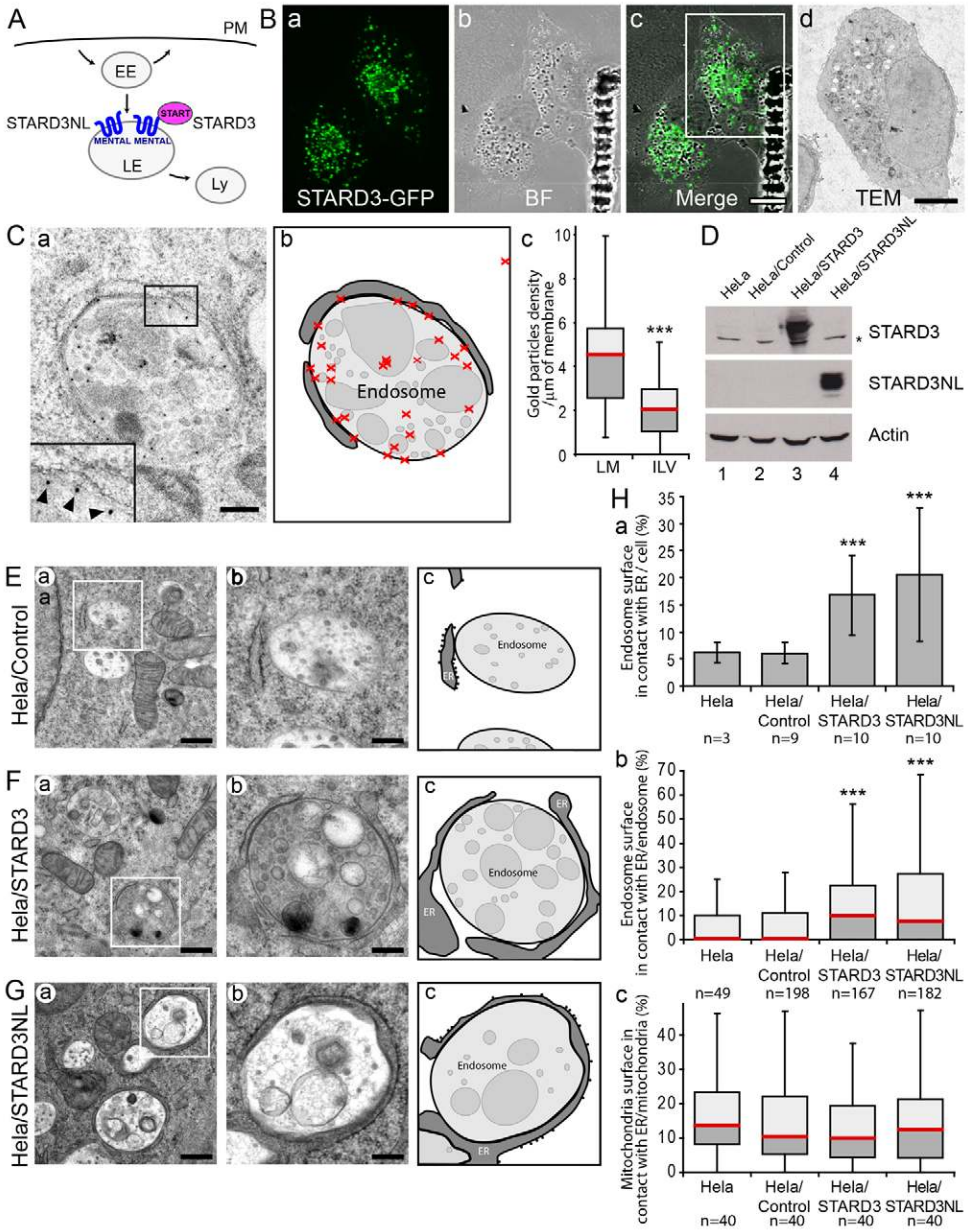

Fig. 1. STARD3 or STARD3NL expression creates extensive MCSs between LEs and the ER. (A) STARD3 and STARD3NL are lipid transfer proteins at the surface of late endosomes (LE). PM, plasma membrane; EE, early endosome; Ly, lysosome. The MENTAL and the START domains are shown in blue and magenta, respectively. (B) Correlative light and electron microscopy. HeLa cells expressing STARD3–GFP were visualized by confocal microscopy (a). Transmitted light bright-field (BF; b) and the merged (c) images are shown. Scale bar: 10 µm. GFP-positive cells were processed for TEM (d) and TEM samples were correlated with their respective fluorescence images. For instance, the cell shown in d is the cell outlined in white in c. Scale bar: 5 µm. (C) Immunogold labeling of STARD3–GFP-positive cells following CLEM. An endosome labeled with anti-GFP antibody is shown (a). Gold-labeled STARD3–GFP is mainly found on the limiting membrane of endosomes. STARD3–GFP-positive endosomes are often tightly surrounded by ER-like structures. A 2× magnification of the area outlined in black is shown in the lower-left corner; arrowheads indicate gold particles. Scale bar: 200 nm. (b) Schematic representation of contacts between organelles shown in panel a with gold particles depicted as red crosses. (c) Box plot of gold particle density (per µm) quantification on the endosome-limiting membrane (LM) and on ILVs ($n=24$ endosomes); box plots show the median of the data in red; the values between the median and the first and the third quartile are in dark and light gray, respectively. The whiskers are set at 1.5×InterQuartile Range (IQR). (D) Western blot analysis of STARD3- or STARD3NL-overexpressing HeLa cells. (E–G) TEM images of control HeLa cells (E) and cells overexpressing STARD3 (F) or STARD3NL (G). (b) 2.5× magnification of the area outlined in white in a. (c) Schematic representation of contacts between organelles shown in b; the ER, endosomes and ILV are in dark, light and medium gray, respectively; ribosomes are represented as small dots lining the ER. Scale bars: 500 nm (a), 200 nm (b). (Ha,b) Quantification by stereology of ER–endosome contacts on TEM sections. (a) Percentage of the total endosome perimeter per cell section in contact with the ER (mean ± s.d.). n: number of cell sections quantified. (b) Percentage of the endosome perimeter in contact with the ER (expressed per endosome; box plot median highlighted in red). n: number of endosome sections quantified.*$P<0.01$ (Mann–Whitney test). (c) Quantification of ER–mitochondria contacts expressed as the percentage of the total mitochondrial perimeter that is in contact with the ER (expressed per mitochondrion; box plot median highlighted in red). n, number of mitochondrial sections quantified.

additional 210 residue START domain, which is a highly conserved domain that forms a lipid binding cavity (Ponting and Aravind, 1999). Each START is specific for certain lipids, and STARD3 is specific for cholesterol (Tsujishita and Hurley, 2000). Previously, we proposed that STARD3 could be involved in an interaction of LEs with distinct organelles (Alpy and Tomasetto, 2005; Alpy and Tomasetto, 2006). In this study, we have used a combination of microscopy approaches to investigate the interaction of STARD3 and STARD3NL with a conserved ER protein at LE–ER MCSs.

Results

STARD3 and STARD3NL create late endosome–endoplasmic reticulum membrane contact sites

To address whether STARD3 is involved in formation of MCSs between LEs and another organelle (Fig. 1A) we observed STARD3-positive endosomes at the ultrastructural level, using correlative light and electron microscopy (CLEM). HeLa cells transiently transfected with a STARD3-GFP-expressing construct were first visualized by confocal microscopy (Fig. 1B). GFP-positive cells were further processed for correlative transmission electron microscopy (TEM), which allowed analysis of the ultrastructure of STARD3–GFP-positive cells only. To gain further information on the localization of STARD3, ultrathin sections from STARD3–GFP-positive cells were then labeled with anti-GFP antibodies (Fig. 1C). In transfected cells, gold particles corresponding to STARD3 were mainly found at the limiting membrane of endosomes and to a lesser extent on intralumenal vesicle (ILV) membranes (Fig. 1C). Quantification revealed that the gold particle density on the endosome limiting membrane was more than twice that on the ILV membrane (Fig. 1Cc). We noted that in STARD3-expressing cells most STARD3-positive endosomes show extensive and tight contacts with an organelle with an ER-like morphology (Fig. 1Ca).

To characterize the contacting organelle, we used high-pressure freezing and freeze substitution to preserve and contrast cellular membranes (Fig. 1E–G). We identified the ER as the organelle in contact with STARD3 (HeLa/STARD3)-positive LEs, as the sheets wrapping LEs were sometimes decorated with ribosomes (see Fig. 1Fb). In control cells (HeLa/Control), endosomes identified by their ILVs had few contacts with the ER that only involved short ER segments (Fig. 1E). In contrast, in HeLa/STARD3 cells, most endosomes were tightly associated with ER membranes that were often wrapped around the organelle (Fig. 1F). In addition, in HeLa/STARD3 cells there were more internal membranes and the ILVs were bigger. Next, to distinguish which domain in STARD3 is involved in ER tethering, we repeated these experiments using HeLa cells stably expressing STARD3NL (HeLa/STARD3NL) because it contains only the MENTAL domain (Fig. 1A,D). HeLa/STARD3NL cells also showed extensive wrapping of ER membranes around endosomes (Fig. 1G) indicating that the START domain does not function in generating the LE–ER MCS. Of interest, ER sheets in contact with endosomes in both cell models were a mixture of smooth ER and rough ER. Indeed in HeLa/STARD3, 64% and 36% of analyzed LEs were covered by smooth and rough ER, respectively ($n=78$, Fig. 1Fb), and similar results were obtained with HeLa/STARD3NL: 60% and 40% of smooth and rough ER respectively ($n=81$, Fig. 1Gb). Ribosomes were not found on membrane opposed directly to the endosome (Fig. 1Gb,c).

To better understand the generation of MCSs, we quantified serial TEM sections stereologically (Mayhew, 1991). STARD3 and STARD3NL expression increased the proportion of LE limiting membrane wrapped by ER to 18% and 20% respectively, compared with 6% in control cells (Fig. 1Ha). The correlate of this for single sections is that in control cells most sectioned endosomes showed no or little contact with the ER, whereas in STARD3- and STARD3NL-expressing cells the majority of sectioned endosomes showed an extended contact with the ER (Fig. 1Hb). Moreover, the number of contacts per endosome section was higher in HeLa/STARD3 (mean ± s.d.: 0.77±0.16; $P<0.01$) and HeLa/STARD3NL cells (0.72±0.13; $P<0.01$) compared with HeLa/Control (0.46±0.1) cells. To look at the specificity of these contacts, we tested whether overexpression of STARD3 or STARD3NL causes ER proliferation, as this might lead to increased interaction with all other organelles (supplementary material Fig. S1). Neither ER density, nor ER stress were increased in HeLa/STARD3 or HeLa/STARD3NL cell lines compared with control cells. Moreover, another MCS of great importance, between the ER and mitochondria, was unaffected by STARD3 or STARD3NL expression (Fig. 1Hc).

Altogether these ultrastructural studies show that STARD3 and STARD3NL have the capacity to induce the formation of MCSs between LEs and the ER.

STARD3 and STARD3NL recruit the ER-resident VAP-A and VAP-B proteins to MCSs

The localization of both STARD3 and STARD3NL within an MCS suggests that these proteins could be part of the molecular machinery responsible for LE–ER tethering. Other types of MCS involving the ER and other organelles use VAMP-associated proteins (VAP proteins) A and B (De Vos et al., 2012; Kawano et al., 2006; Rocha et al., 2009), which are membrane-bound ER-resident proteins (Skehel et al., 2000). VAP-A and VAP-B have been shown to interact with specific peptide motifs called FFAT motifs (two phenylalanines in an acidic tract) (Loewen et al., 2003). The direct interaction between VAP-A or VAP-B in the ER with FFAT-containing proteins docked on membranes of other organelles was proposed as a general mechanism to allow targeting of proteins to MCSs (Levine and Loewen, 2006; Loewen et al., 2003). We therefore hypothesized that STARD3 and STARD3NL could directly interact with VAP proteins at an LE–ER MCS. To address this, we searched for a FFAT motif in the MENTAL domain. The analysis of the primary sequences of STARD3 and STARD3NL from different metazoan species (Fig. 2A) revealed the presence of a conserved FFAT-like motif at the C-terminal end of the MENTAL domain. Like other FFAT-like motifs, this motif is centered on two aromatic residues with an adjacent tract of acidic amino acids (Mikitova and Levine, 2012). However, this motif differs from most other FFAT motifs as the acidic tract does not precede but follows the FF.

The presence of a FFAT-like motif in the MENTAL domain supports the notion that STARD3 and STARD3NL interact with VAP to create the MCS. To test this possibility, we examined the ability of STARD3 to redistribute VAP. As a control, we first expressed a generic ER marker tagged with GFP (GFP-ER) in HeLa cells (Fig. 2Ba). This GFP-ER probe exhibited a typical ER reticular pattern extending throughout the cytoplasm with a perinuclear enrichment corresponding to the nuclear envelope. When co-expressed with STARD3, the GFP-ER marker had a predominantly homogeneous reticular pattern (Fig. 2C).

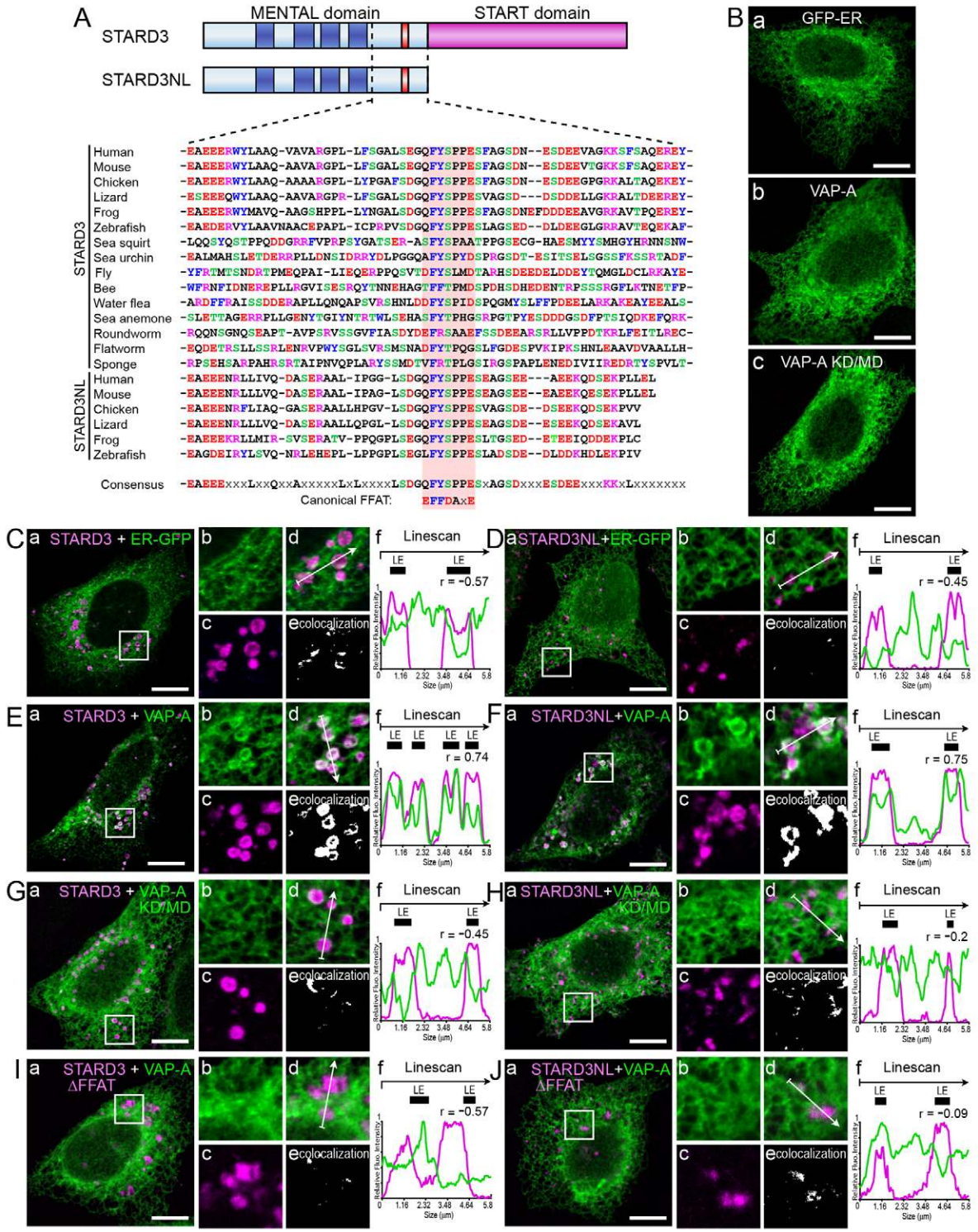

Fig. 2. STARD3 and STARD3NL recruit the ER-resident VAP-A and VAP-B proteins to LE–ER MCS. (A) Schematic representation of STARD3 and STARD3NL. Transmembrane helices and the FFAT motif are in dark blue and red, respectively. The alignment of the C-terminus of the MENTAL domain of STARD3 and STARD3NL from different species (see Materials and Methods) is shown below. Acidic (DE), basic (KR), alcoholic (ST) and aromatic (FWY) residues are in red, magenta, green and blue, respectively. The consensus sequence is shown at the bottom together with the canonical FFAT-motif sequence (Loewen et al., 2003). (B) WT (b) and mutant (KD/MD; c) GFP–VAP-A are localized similarly to the GFP-ER probe (a) in HeLa cells. (C–H) Co-expression of STARD3 (C,E,G; magenta) or STARD3NL (D,F,H; magenta) and GFP-ER (C,D; green), VAP-A (E,F; green) or mutant VAP-A KD/MD (G,H; green). (I,J) Co-expression of mutant STARD3 (I; magenta) or mutant STARD3NL (J; magenta) lacking their FFAT motifs (ΔFFAT) and VAP-A (I,J; green). All of C to J shows six subpanels: (a) Merged image of green and magenta signals. Scale bars: 10 µm. (b–d) Higher magnification (3×) of the area outlined in white in a, showing the green (b), magenta (c) and merge (d) signals. (e) Pixels where the green and the magenta channels co-localize are shown in white. (f) Linescan analyses with relative fluorescence intensities of the magenta and green channels along the arrow in d. Black rectangles indicate the positions of LEs.

Occasionally, areas of colocalization of GFP-ER and STARD3 signals, corresponding probably to LE–ER MCS, were observed (Fig. 2Ce). Given that the ER contains more membrane than any other organelle, even if endosomes were entirely covered with ER, we would not expect a generic marker such as GFP-ER to strongly distinguish MCS from the bulk of the ER. In contrast, a specific interaction of VAP proteins with STARD3 should concentrate VAP proteins in ER-endosome MCS. We therefore analyzed the localization of VAP-A tagged with GFP. When expressed in HeLa cells, VAP-A protein exhibited a typical ER distribution similar to the GFP-ER probe (Fig. 2Bb). However, in cells co-overexpressing STARD3, GFP–VAP-A localization was dramatically modified, being concentrated around STARD3-positive endosomes at the expense of the remainder of the ER (Fig. 2E). A high degree of co-localization between VAP-A and STARD3 was found (Fig. 2Ee); in addition, line scans showed that the VAP-A signal peaked at the site of STARD3 in the limiting membrane of LEs (Fig. 2Ef). By comparison, the generic GFP-ER marker showed only a modest ER enrichment around STARD3-positive organelles (Fig. 2Ce). These results show that VAP-A is recruited to LE–ER MCSs generated by STARD3.

To evaluate whether the FFAT-binding ability of VAP-A was required for its recruitment around STARD3-positive endosomes, we performed similar experiments using mutant VAP-A. Several residues of VAP-A and VAP-B are crucial for the interaction with FFAT motifs (Kaiser et al., 2005; Loewen and Levine, 2005). The K94D M96D mutation of VAP-A and the K87D M89D mutation of VAP-B (hereafter both referred as KD/MD mutants) were shown to abolish FFAT binding (Kaiser et al., 2005). When expressed in HeLa cells, VAP-A KD/MD had a typical ER pattern similar to WT VAP-A (Fig. 2Bc). However, unlike WT VAP-A, VAP-A KD/MD remained evenly distributed throughout the ER in cells overexpressing STARD3 (Fig. 2G). This result shows that the recruitment of VAP-A to STARD3-induced LE–ER MCSs requires its ability to bind FFAT-motifs. We also documented the specific recruitment of wild-type VAP-A around STARD3 LE using time-lapse microscopy in live cells (STARD3–mCherry with VAP-A–GFP; supplementary material Movie 1 and VAP-A KD/MD-GFP; supplementary material Movie 2).

As STARD3 possesses a FFAT-like motif, we made a reciprocal study and evaluated whether this motif was required for VAP recruitment in LE–ER MCSs. We removed seven residues (QFYSPPE) from the STARD3 FFAT motif by mutagenesis (STARD3 ΔFFAT) and co-expressed this mutant protein with WT VAP-A. Deletion of the FFAT-like motif in STARD3 was sufficient to abolish VAP-A accumulation around endosomes (Fig. 2I) thus indicating that the interaction between VAP-A and the STARD3 FFAT motif is necessary for the recruitment of VAP-A to LE–ER MCSs.

Given that a conserved FFAT-like motif is also present in STARD3NL, we then looked at the effect of STARD3NL on VAP-A recruitment in STARD3NL-induced LE–ER MCSs. First, we verified that the expression of STARD3NL had no major effect on ER morphology. Indeed, the GFP-ER probe exhibited a typical ER reticular pattern extending throughout the cytoplasm in cells expressing STARD3NL (Fig. 2D). However, similarly to STARD3, STARD3NL induced a massive concentration of VAP-A around LEs (Fig. 2F), and this recruitment was dependent upon VAP-A binding to FFAT motifs (Fig. 2H) and on the presence of a FFAT motif in STARD3NL (Fig. 2J). To further substantiate these observations, we looked at endogenous VAP-A protein in control and STARD3NL-expressing cells (supplementary material Fig. S2A,B). Interestingly, endogenous VAP-A localizes generally throughout the ER, whereas it accumulated around STARD3NL-positive endosomes in HeLa/STARD3NL cells. Together, these results indicate that the interaction of VAP-A with STARD3NL FFAT motif leads to its recruitment into LE–ER MCSs.

Considering that VAP-A and VAP-B are closely related and have redundant functions (Lev et al., 2008), we next examined whether STARD3 and STARD3NL also recruit VAP-B to LE–ER MCS. As expected, VAP-B was recruited to LE–ER MCSs in STARD3- and STARD3NL-expressing cells, and this localization of VAP-B was dependent on its ability to bind FFAT motifs and on the presence of a FFAT motif in STARD3 or STARD3NL (supplementary material Fig. S2C–I). Altogether, these results show that STARD3 and STARD3NL induce the recruitment of VAP proteins to LE–ER MCSs.

STARD3 interacts with VAP-A in live cells

These colocalization experiments supported the notion that VAP proteins directly interact with STARD3 and STARD3NL FFAT motifs at MCSs. Next, we tested this interaction in live cells using FRET, which occurs at a close proximity (~1–10 nm). To determine whether the two proteins interact, we performed fluorescence lifetime imaging microscopy (FLIM), which detects FRET between the donor and acceptor fluorophores, here GFP and mCherry, respectively (Fig. 3A). Under FRET-FLIM conditions, proximity between the two proteins will decrease the GFP fluorescence lifetime (Llères et al., 2009). First, we determined the fluorescence lifetime of GFP–VAP-A expressed alone in HeLa cells. A map of GFP fluorescence lifetime (τm) shows that GFP fluorescence lifetime was homogeneous across cells (Fig. 3B, mean=2.32 nseconds). In contrast, when STARD3–mCherry was co-expressed with GFP–VAP-A, the τm map shows several localized lifetime minima (Fig. 3B). The global τm decrease is illustrated by the shift of GFP fluorescence lifetime distribution (Fig. 3Bc). Interestingly, at the subcellular level the positions of lifetime decreases coincided with the position of STARD3–mCherry-positive endosomes, indicating that VAP-A and STARD3 interact at these sites. When the same experiment was performed with the KD/MD VAP-A mutant, the fluorescence lifetime measured for GFP–VAP-A KD/MD was unchanged in the presence of STARD3–mCherry, indicating a lack of interaction (Fig. 3B, mean=2.31 nseconds). To quantify interaction in live cells, we measured the percentage of pixels with a low τm (τm <2.215 nseconds) in the different samples. In cells expressing GFP–VAP-A alone or GFP–VAP-A KD/MD (alone or with STARD3–mCherry) less than 5% of pixels had low τm. In contrast, in cells expressing both GFP-VAP-A and STARD3-mCherry more than 20% of the pixels exhibited low τm (Fig. 3C).

Altogether, these results show that STARD3 and VAP-A interact in live cells in discrete portions of the ER that correspond to membrane contact sites between the ER and LE.

STARD3 and STARD3NL form complexes with VAP-A and VAP-B proteins

To directly assess whether STARD3 and STARD3NL interact with VAP-A or VAP-B, we performed co-immunoprecipitation experiments following *in vivo* cross-linking. FLAG-tagged STARD3 was co-expressed in HeLa cells with WT or KD/MD

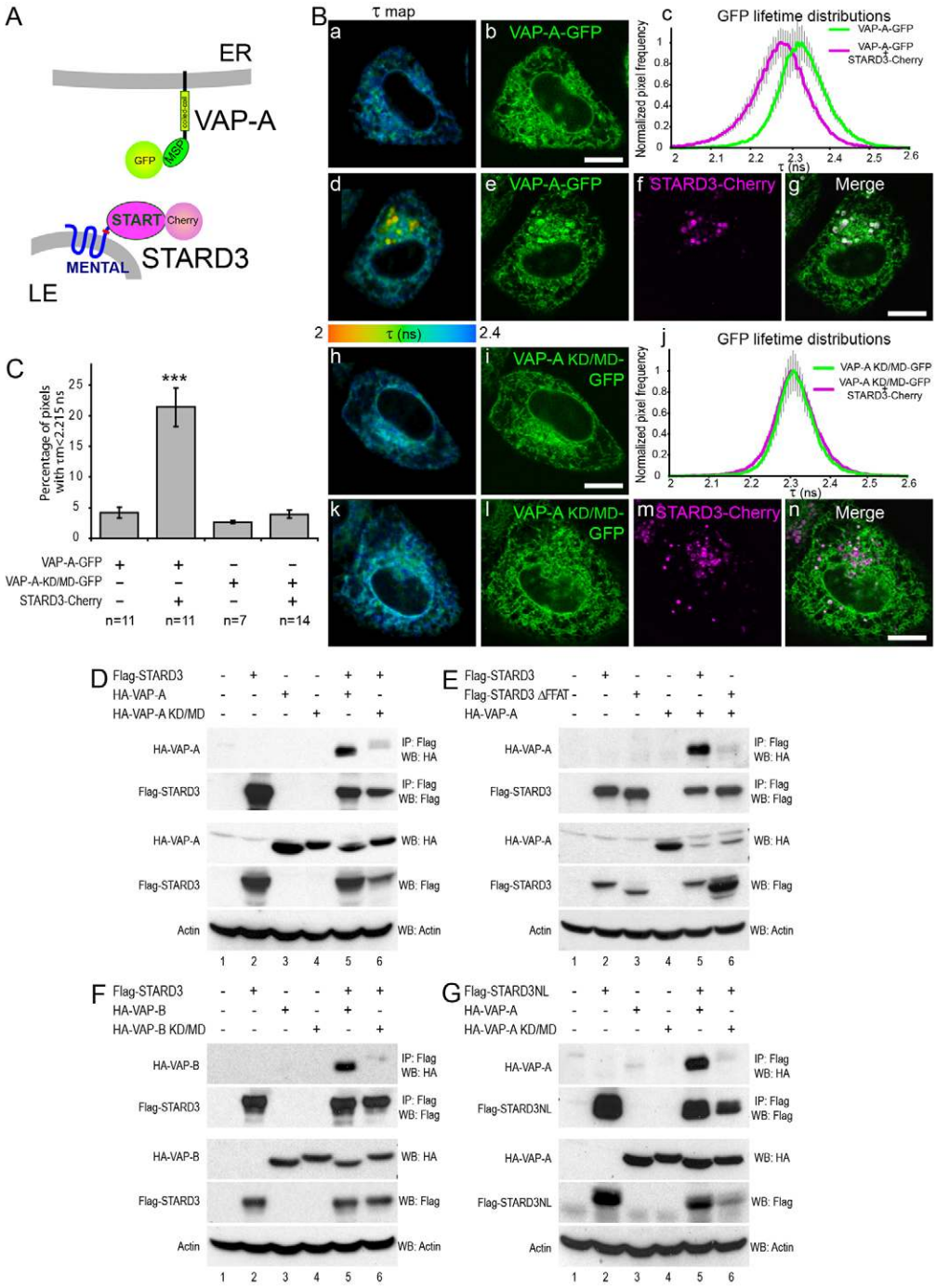

Fig. 3. STARD3 and STARD3NL interact with VAP proteins in a FFAT-motif-dependent manner. (A) Scheme of the VAP-A–GFP and STARD3–mCherry fusion proteins used for FRET-FLIM experiments. (B) FRET-FLIM analysis of live cells expressing GFP–VAP-A alone (a–b), GFP–VAP-A and STARD3–mCherry (d–g), GFP–VAP-A KD/MD alone (h,i) or GFP–VAP-A KD/MD and STARD3–mCherry (k–n). Cells were imaged by confocal microscopy (b, e–g, i, l–n) followed by FLIM (a, d, h and k). The spatial distribution of the mean fluorescence lifetime of the GFP donor (τm map) is displayed using a continuous pseudocolor scale ranging from 2 to 2.4 nseconds (a, d, h and k). (c) Mean lifetime distribution curves (± s.e.m.) of GFP–VAP-A (n=11 cells/sample). (j) Mean lifetime distribution curves (± s.e.m.) of GFP–VAP-A KD/MD (n=7 cells for GFP–VAP-A KD/MD alone, n=14 for GFP–VAP-A KD/MD + STARD3–mCherry). Scale bars: 10 µm. (C) Percentage±s.d. of GFP-positive pixels with a GFP fluorescence lifetime below 2.215 ns. (D,E) Immunoprecipitation experiments after *in vivo* cross-linking between STARD3 and VAP-A testing the effect of mutating either VAP-A KD/MD (D) or STARD3 ΔFFAT (E). (F,G) Immunoprecipitation experiments after *in vivo* cross-linking between STARD3 and VAP (as in D,E) testing the effect of substituting either VAP-B (F) or STARD3NL (G). In D–G inputs were 1/10th of the cell extract.

mutant VAP-A (Fig. 3D). VAP-A was co-immunoprecipitated with STARD3 but the KD/MD mutant form of VAP-A was not (Fig. 3D). This shows that VAP-A interaction with STARD3 requires its FFAT recognition motif. Reciprocally, we performed co-immunoprecipitation experiments between VAP-A and WT or the ΔFFAT STARD3. Consistently, whereas STARD3 and VAP-A were co-immunoprecipitated (Fig. 3E), the STARD3 mutant lacking the FFAT motif did not interact with VAP-A. Thus, STARD3 interacts with VAP-A in a FFAT-motif-dependent manner.

Based on the sequence similarities between VAP-A and VAP-B, we predicted that VAP-B would interact similarly with STARD3, and tested its binding to STARD3 (Fig. 3F). Indeed, VAP-B was co-immunoprecipitated with STARD3 whereas the KD/MD mutant form of VAP-B was not. This shows that both VAP-A and VAP-B interact with STARD3 and that the ability of VAP-B to bind FFAT motifs is necessary for this interaction. Because a FFAT-like motif is present in STARD3NL (Fig. 2A), we performed similar co-immunoprecipitation experiments with VAP-A and STARD3NL (Fig. 3G). Consistent with the FFAT-like motif sequence conservation between STARD3 and STARD3NL, STARD3NL was also co-immunoprecipitated with VAP-A.

Collectively, these results show that STARD3 and STARD3NL have bona fide FFAT-like motifs in the C-terminal ends of their MENTAL domain that interact with VAP across LE–ER MCS.

LE–ER MCS formation by STARD3NL relies on the presence of VAP proteins

To further substantiate the role of VAP proteins, we investigated whether their presence was required for the formation of STARD3- and STARD3NL-induced LE–ER MCSs. We knocked down VAP-A and VAP-B using two different small hairpin RNAs (shRNA) in HeLa cells expressing STARD3NL. Compared to non-silenced cells (HeLa/STARD3NL/shCtrl), VAP-A and VAP-B levels were reduced to 6% and 50% with one set of shRNAs, and 13% and 3% with the other set (Fig. 4A). After processing cells for TEM, cells knocked down for VAP-A and VAP-B exhibited only rare and short LE–ER contacts (Fig. 4C,D, a–c), whereas HeLa/STARD3NL/shCtrl cells showed extensive LE–ER MCSs (Fig. 4Ba–c), similarly to what was observed in HeLa/STARD3NL (Fig. 1). Quantification of contact sites confirmed that knockdown of VAP-A and VAP-B dramatically reduced the number and size of MCSs (Fig. 4E). It should be noted that similarly to HeLa/STARD3NL cells (Fig. 1), HeLa/STARD3NL cells knocked down for VAP-A and VAP-B exhibited ILV morphological defects that appeared unrelated to the formation of LE-RE contacts (Fig. 4C,D). These results show that STARD3NL-mediated LE–ER MCS formation requires the expression of VAP proteins.

ER sheets closely wrap endosome membrane

To better appreciate the spatial relationship between endosome and ER membranes at MCSs, we performed electron tomography on semi-thin sections (~200 nm) of HeLa/STARD3NL cells (Fig. 5; supplementary material Movie 3). This analysis confirmed that regions of the ER typically form extended contacts with LEs (Fig. 5A). Moreover, we could observe continuities between ER tubules and ER sheets wrapping the

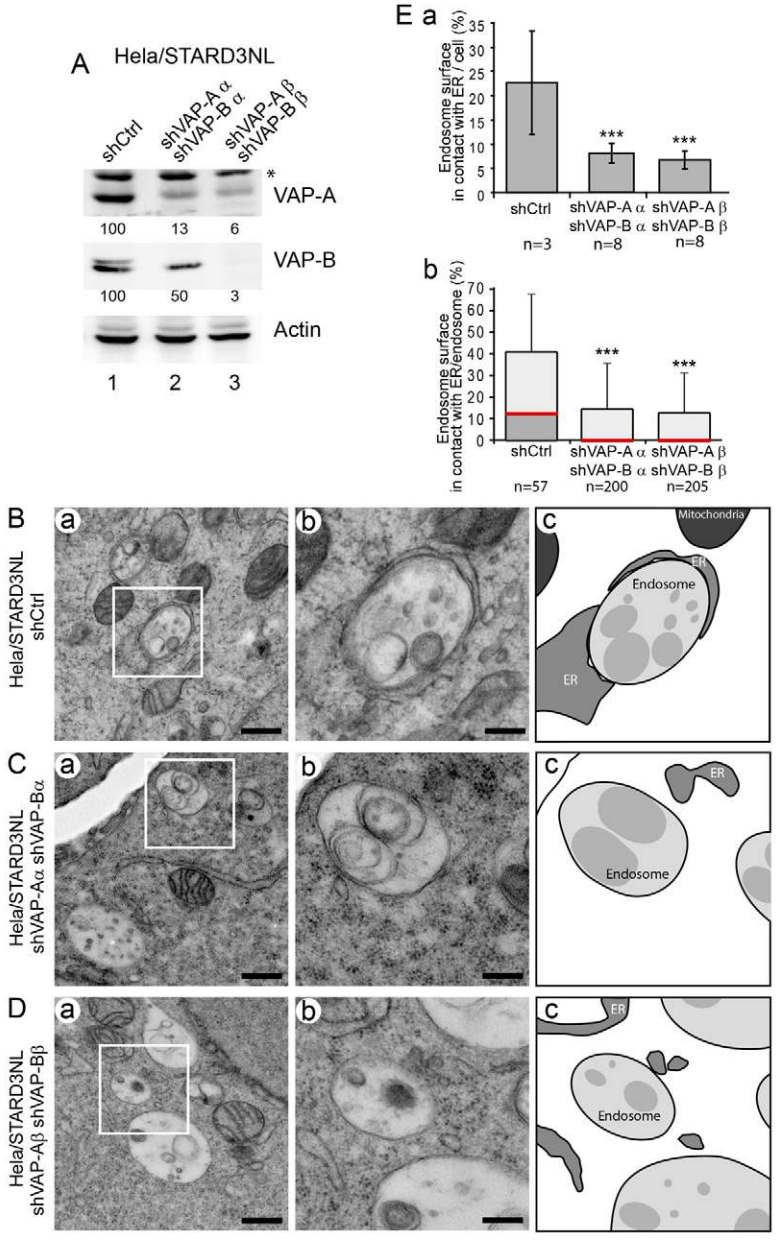

Fig. 4. LE–ER MCS formation relies on the presence of VAP proteins. (A) Western blot analysis of VAP-A and VAP-B in HeLa/STARD3NL cells expressing a control shRNA (shCtrl) or two pairs of shRNAs targeting VAP-A and VAP-B (shVAP-Aα/shVAP-Bα or shVAP-Aβ/shVAP-Bβ). Relative protein levels are shown below each blot (percentage compared to HeLa/shCtrl cells). *non-specific band. (B–D) TEM images of HeLa/STARD3NL shCtrl (B), HeLa/STARD3NL shVAP-Aα/shVAP-Bα (C) or shVAP-Aβ/shVAP-Bβ (D) cells. (b) Magnification (2.5×) of the area outlined in white in a. (c) Schematic representation of contacts between organelles shown in b. Scale bars: 500 nm (a); 200 nm (b). (E) Quantification by stereology of ER–endosome contacts on TEM sections. (a) Percentage of total endosome perimeter per cell section in contact with the ER (mean ± s.d). *n*=number of cell sections quantified. (b) Percentage of endosome perimeter per endosome in contact with the ER (box plot with median highlighted in red). *n*=number of endosome sections quantified.*$P<0.01$ (Mann–Whitney test).

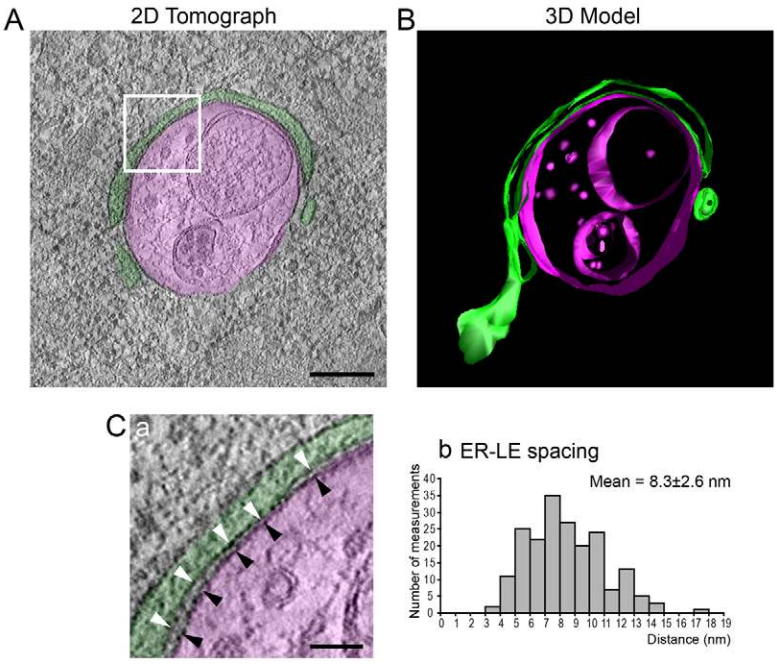

Fig. 5. 3D structural analysis of MCS. (A) Two-dimensional tomograph obtained from a 200 nm thick section of HeLa/STARD3NL cells showing an endosome (magenta) wrapped by the ER (green). Scale bar: 100 nm. (B) A three-dimensional model of A. (C,a) High magnification of the boxed area in A., showing the distance between the ER membrane (white arrowheads) and the limiting membrane of the endosome (black arrowheads). Scale bar: 50 nm. (b) Distances measured between the contacting ER and LE membranes ($n=13$ different endosomes acquired by electron tomography).

LE (Fig. 5B). The high resolution of this technique allowed us to measure the distance between the limiting membrane of LEs and the contacting ER membrane as 8.3 nm ($n=13$, range 3–15 nm; Fig. 5C), which indicates a very tight wrapping of endosomes by the ER.

Overexpression of STARD3NL protein inhibits generation of LE tubules

The endocytic pathway sorts internalized cargo to different destinations, including the plasma membrane, trans-Golgi network and lysosomes (Pfeffer, 2003; Russell et al., 2006; Trowbridge et al., 1993). Previous studies have reported that STARD3 overexpression alters the morphology of the endosomal system (reviewed by Alpy and Tomasetto, 2006). Notably, increased levels of STARD3 were associated with the presence of enlarged and less mobile LE (Alpy et al., 2005; Hölttä-Vuori et al., 2005; Liapis et al., 2012; Zhang et al., 2002), and we showed that this alteration was independent of the cholesterol transfer activity of STARD3, because the same effect occurred with STARD3NL (Alpy et al., 2005; Alpy et al., 2002). Given that both STARD3 and STARD3NL are ER–endosome tethers, we reasoned that the creation of extended LE–ER contacts by STARD3 or STARD3NL might cause LE enlargement and loss of mobility. To address this, endosome size was compared in control cells and in cells expressing WT STARD3NL and a STARD3NL mutant devoid of the FFAT motif (supplementary material Fig. S3). Consistent with previous studies, expression of STARD3NL caused enlargement of LAMP1-positive endosomes and lysosomes, with a high degree of VAP-A colocalization (supplementary material Fig. S3C), indicating extended ER–endosomes contacts. Strikingly, in cells expressing a truncated STARD3NL mutant lacking its FFAT motif so that no colocalization with VAP-A was induced, the LAMP1-positive compartment was still significantly enlarged (supplementary material Fig. S3D,E). This indicates that enlargement of the endocytic compartment upon STARD3NL overexpression is not caused by endosome contact with the ER, but by another activity of the MENTAL domain.

The endo-lysosomal network is characterized by interconnected vacuolar and tubular elements (Sachse et al., 2002). To test whether promoting ER–endosome contacts by STARD3NL expression would regulate the dynamics of this network, we next followed endocytic dynamics by live-cell imaging in cells under three conditions: (1) extended MCS (HeLa/STARD3NL-GFP/shCtrl); (2) controls without MCS (HeLa/STARD3NL-GFP/shVAP-A shVAP-B); (3) a separate endocytic marker as control (HeLa/LAMP1-GFP). Both STARD3NL-positive and LAMP1–GFP positive compartments displayed short- and long-range stochastic movements, and vesicle-to-tubule transitions. In control cells, clearly defined tubular carriers formed, frequently containing either of the endocytic marker we studied (Fig. 6A,C,D; supplementary material Movies 4 and 6). However, in cells making LE–ER contacts through overexpressed STARD3NL binding to endogenous VAP, tubular carriers were shorter and far fewer in number (Fig. 6B,D; supplementary material Movie 5).

Together, these data establish that the extensive LE–ER contacts mediated by the presence of STARD3, STARD3NL and VAP proteins alter endosomal dynamics.

VAP proteins, STARD3 and STARD3NL mark endogenous LE–ER MCSs that appear to be independent of the presence of ORP1L and PTP1B

To date it has been beyond the limit of detection to document the presence of endogenous protein bridges spanning the LE–ER MCS. Indeed, localizing any protein expressed at endogenous levels to any mammalian MCS has been a great challenge that has held back the entire field (Helle et al., 2013). One reason for this is that a protein such as VAP has many partners, some on LEs, others on the plasma membrane, mitochondria and trans-Golgi network (Lev et al., 2008). Only a small proportion is likely to bridge one class of MCSs, and this may not be

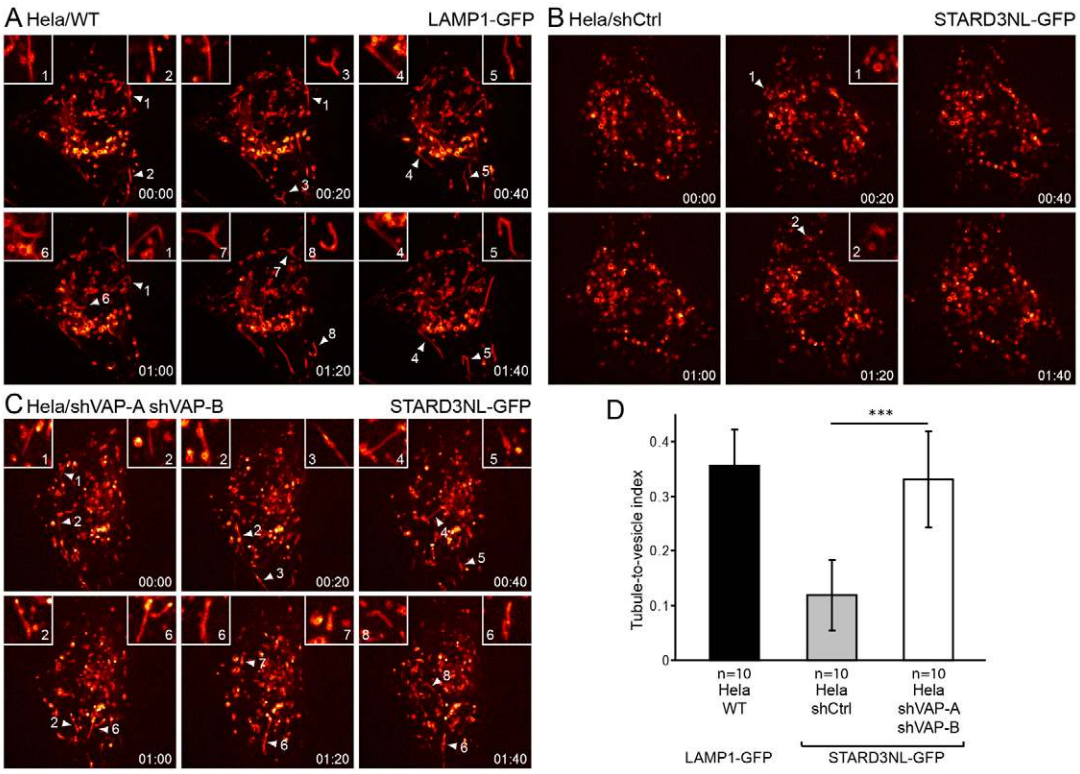

Fig. 6. The presence of LE–ER contacts prevents vesicle-to-tubule transitions. (A) Frames of time-lapse imaging of endosomes labeled with LAMP1–GFP from WT HeLa cells (see supplementary material Movie 4). (B,C) Frames of time-lapse imaging of endosomes labeled with STARD3NL–GFP, in cells making extended MCSs (B; HeLa/shCtrl; see supplementary material Movie 5) and in cells devoid of these MCSs (C; HeLa/shVAP-Aβ/shVAP-Bβ; supplementary material Movie 6). Arrowheads indicate the presence of tubules, insets show a 2× magnification of these tubules. (D) Quantification of the tubule-to-vesicle ratio per cell during a 2-minute recording (n=number of analyzed cells per sample; means ± s.d.).

detectable against a high background of widespread ER elements. To overcome this problem, we applied the recently developed, highly sensitive technique of *in situ* proximity ligation assay (PLA) to the LE–ER MCS (Söderberg et al., 2006). With this assay, proximity (<40 nm) between two proteins is revealed by fluorescent dots. Using antibodies to endogenous STARD3, STARD3NL and VAP-A proteins (since VAP-A is more highly expressed than VAP-B in HeLa cells as analyzed by RT-qPCR; data not shown), we demonstrated proximity between LE and ER markers. Many PLA-positive fluorescent dots were seen in untreated cells, indicating the presence of MCSs (Fig. 7B,C). In contrast, only a few dots were formed in cells knocked down for VAP-A, confirming the specificity of the antibody used for PLA (Fig. 7A–C). We next determined the position of the PLA dots: they were typically excluded from the cell nucleus (supplementary material Movie 7), and they colocalized with the endosome/lysosome marker LAMP1 (Fig. 7D,E). Thus, this experiment shows that endogenous STARD3 and VAP-A interact and create MCSs in HeLa cells.

It has been previously shown that the oxysterol-binding-protein-related 1 (ORP1L) induces the formation of LE–ER membrane contacts by interacting with VAP (Rocha et al., 2009). Through an interaction with Rab7, ORP1L is recruited to LEs where it senses cholesterol levels and regulates endosome positioning. Besides ORP1L, the protein tyrosine phosphatase 1B (PTP1B), an integral ER membrane protein interacts with epidermal growth factor receptor (EGFR) at endosome–ER MCSs (Eden et al., 2010). To determine whether the LE–ER contacts formed by STARD3 and STARD3NL rely on either of these proteins, we measured MCS formation by endogenous STARD3, STARD3NL and VAP proteins in cells silenced for either ORP1L or PTP1B (Fig. 7F–H). Silencing of ORP1L and PTP1B was very efficient, as less than 15% of proteins remained (Fig. 7F), but STARD3/VAP-A and STARD3NL/VAP-A contacts were not affected, as similar numbers of PLA-positive dots were detected (Fig. 7G,H).

These experiments show that endogenous LE–ER MCSs can be identified using endogenous STARD3, STARD3NL and VAP-A proteins. They also raise the possibility that this LE–ER bridging complex is distinct from others discovered previously, and so is probably involved in separate cellular functions.

Discussion

In this study, we identified a novel molecular complex that bridges between late endosomes and the endoplasmic reticulum. Overexpression of the LE proteins STARD3 or STARD3NL induces the formation of extended MCSs between LEs and the ER. A conserved FFAT-like motif, identified in the primary sequences of both LE proteins, interacts with VAP-A and VAP-B, homologous proteins on the cytosolic face of the ER. Accordingly, expression of STARD3 or STARD3NL concentrates VAP-A and VAP-B into portions of the ER surrounding LEs. The interaction across the MCS was substantiated by FRET-FLIM and co-immunoprecipitation. Taken together, these results show that STARD3 and STARD3NL

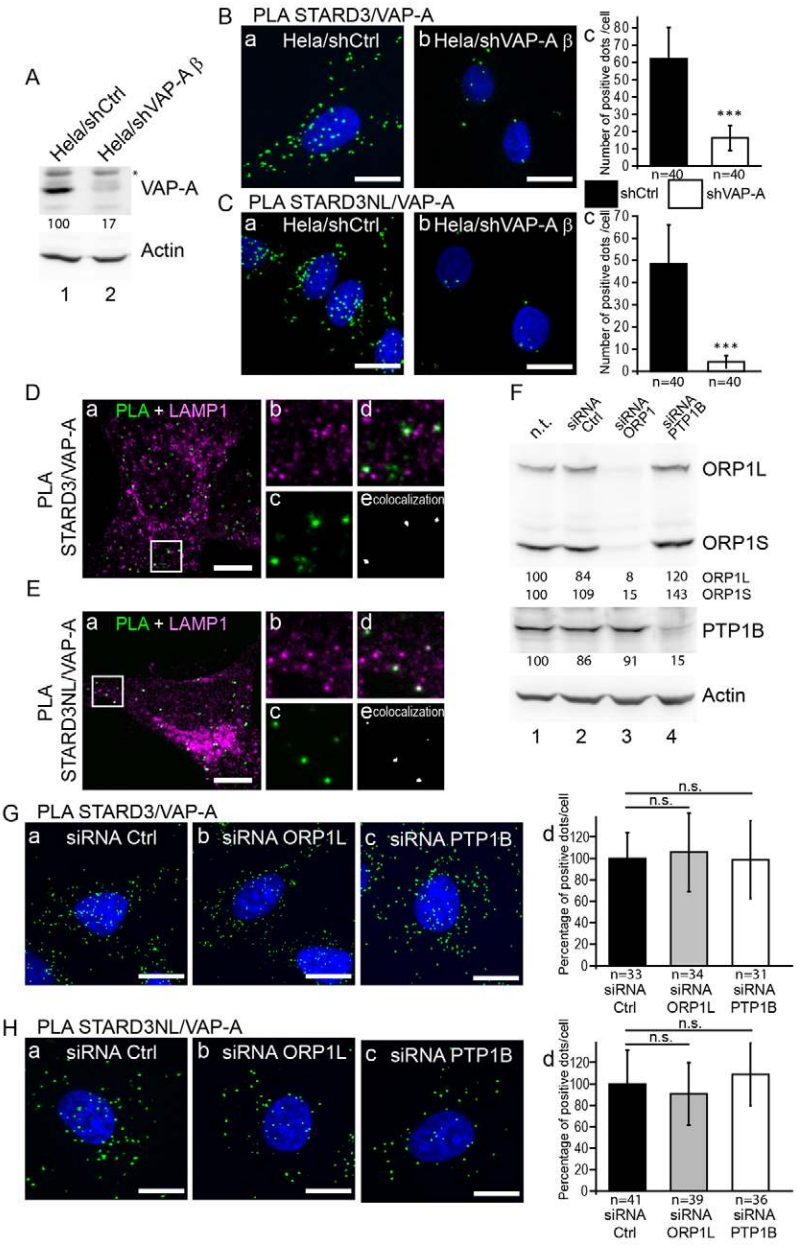

Fig. 7. Endogenous LE–ER contacts are marked by the interaction of STARD3 or STARD3NL and VAP proteins and are formed independently of ORP1L and PTP1B. (A) Western blot analysis of VAP-A expression levels in HeLa cells expressing a control shRNA (shCtrl) or a shRNA targeting VAP-A (shVAP-Aβ). *non-specific band. (B,C) *In situ* proximity ligation assay (PLA; green) performed on endogenous STARD3 and VAP-A (B) or endogenous STARD3NL and VAP-A (C) in HeLa shCtrl (a) and HeLa shVAP-A cells (b). Nuclei are stained blue. (c) PLA dots quantification per cell (n=40 cells per sample; means ± s.d.). Scale bars: 15 µm. (D–E) PLA (green) performed on endogenous STARD3 and VAP-A (D) or endogenous STARD3NL and VAP-A (E) in HeLa cells labeled with anti-LAMP1 (magenta). Merged images of green and magenta signals. (b–d) Higher magnification (3×) of the area outlined in white in a, with magenta (b), green (c) and merged (d) signals. (e) Colocalized pixels from the green and the magenta channels of the magnified area are shown in white. Scale bars: 15 µm. (F) Western blot analysis of ORP1L and PTP1B expression levels in cells silenced with control or specific siRNA pools. Relative protein levels are shown below each blot (percentage compared to parental cells). (G,H) PLA on STARD3 (G), STARD3NL (H) and VAP-A in control (a), ORP1L (b)- and PTP1B (c)-silenced cells. The quantification of PLA dots per cell is indicated in d (n=number of analyzed cells per sample; means ± s.d.). Scale bars: 15 µm.

on the limiting membrane of LE interact with VAP on the ER at sites of close membrane apposition between these two organelles. Finally, by using an *in situ* proximity ligation assay we were able to detect the endogenous proteins forming LE–ER contacts, which has not been possible for any LE–ER contact previously.

The spacing between LE and ER membranes (8.3 nm) was narrow and compatible with the presence of relatively small protein complexes such as those formed by the interaction between STARD3 or STARD3NL and VAP. The FFAT motifs in STARD3 and STARD3NL are located on the cytoplasmic face of LE membranes close to the membrane anchored MENTAL domain (Alpy et al., 2001; Alpy et al., 2002); therefore, we would predict an inter-membrane spacing determined almost solely by the cytoplasmic region of VAP, which associates a coiled-coil (28 aa), an extended region (40 aa) and the superimmunoglobulin fold MSP domain (Kaiser et al., 2005; Nishimura et al., 1999). Together these are predicted to occupy a space 5–10 nm wide, which is compatible with the spacing we measured at LE–ER MCSs (Fig. 8).

The ER interaction partners of STARD3 and STARD3NL in LE–ER MCS are VAP-A and VAP-B. Interestingly, VAP proteins were shown to homo- and hetero-dimerize (Nishimura et al., 1999) which is also the case for STARD3 and STARD3NL (Alpy et al., 2005); it is, therefore, likely that the molecular complexes formed by these proteins involve at least four proteins, and may even form large oligomers. We can speculate that these interactions could modulate contacts between the ER and LEs.

Other molecular bridges have been ascribed to the LE–ER MCSs. Our results suggest that the molecular tether formed by STARD3, STARD3NL and VAP proteins differs from the two established ones, which involve ORP1L–VAP and EGFR–PTP1B. Silencing either ORP1L or PTP1B does not prevent STARD3 or STARD3NL promoting ER–endosome contacts. This result suggests that several bridging complexes target the

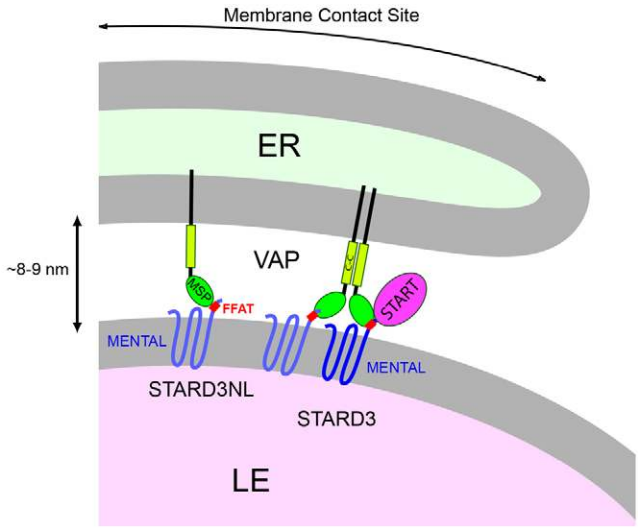

Fig. 8. Schematic representation of protein organization within LE–ER MCSs. Molecular machinery consisting of STARD3, STARD3NL and VAP proteins which tethers the limiting membrane of the LE and the ER.

same MCS, as for the ER–plasma membrane contact site (Manford et al., 2012). However, the different bridging complexes might work independently and regulate different cellular functions. The bridge containing ORP1L also contains VAP (Rocha et al., 2009), but the fact that ORP1L is not anchored into endosome membranes suggests that it mediates a more labile tethering between the ER and LE. Recently, it was proposed that STARD3 and ORP1L are present in two LE subpopulations (van der Kant et al., 2013), which is consistent with our experiments showing that silencing of ORP1L did not modify STARD3-induced ER–LE contacts. Of interest, another START protein, CERT (ceramide transfer protein or STARD11), was proposed to function at contact sites. CERT efficiently transports ceramides from the ER to the Golgi apparatus (Hanada et al., 2003), and this lipid transfer was proposed to specifically occur at MCSs between these two organelles (Hanada et al., 2009; Kawano et al., 2006). However, evidence showing that CERT/STARD11 targets ER–Golgi MCSs and that lipid exchange occurs at this site is still missing. This is a good example of the difficulty in direct observation of proteins at MCSs, a problem that we have solved in this case using PLA.

Given the presence of a START domain in STARD3, it was tempting to speculate that STARD3 mediates or regulates lipid transfer at these LE–ER MCSs. However, many lines of evidence, including from this study, indicate that STARD3-mediated LE–ER contacts are built and function independently of the lipid transfer function of this protein. Firstly, STARD3 seems not to be involved in cholesterol exit from late endosomes because its overexpression does not increase ACAT-mediated cholesterol esterification in the ER (Liapis et al., 2012). Secondly, STARD3 and STARD3NL can equally mediate the formation of LE–ER MCSs. Thirdly, overexpression of STARD3 is known to induce perinuclear clustering of enlarged LEs whereas its silencing results in the peripheral dispersion of endosomes (Alpy et al., 2005; Hölttä-Vuori et al., 2005; Liapis et al., 2012; Zhang et al., 2002), and these effects cannot be attributed to the formation of LE–ER MCSs.

STARD3 was recently proposed to be involved in cholesterol transport between LE and the plasma membrane (van der Kant et al., 2013). Although we cannot rule out this possibility, our data support a model in which STARD3 is primarily involved in cholesterol exchange and/or sensing between LEs and the ER.

Live-cell imaging enabled us to reveal an unanticipated function of these STARD3- and STARD3NL-mediated LE–ER tethers. Indeed, they alter vesicle-to-tubule transitions at the LE level, an effect that may be linked to changes in membrane lipid composition or to a blockade of motors that pull on endosomes due to ER binding. The role of vesicle-to-tubule transitions remains elusive. It was reported that there is a co-ordination between endosomal maturation and tubular-based sorting (van Weering et al., 2012). Interestingly, endosome maturation was recently correlated with an increase of endosome–ER contacts (Friedman et al., 2013); this increase of ER-endosome contacts from early to late endosomes might originate from the presence of STARD3 and STARD3NL in LEs. Further work is needed to delineate a possible role of STARD3 and STARD3NL during endosomal maturation. However, it remains possible that the effect on LE dynamics that follows STARD3 and STARD3NL overexpression might simply result from wrapping endosomes extensively in ER.

In this study, we have addressed the subject of connections between the ER and other organelles. Many bridging molecules have been postulated, but very few have so far been identified (de Brito and Scorrano, 2008). The ER can be considered as an intracellular web extended throughout the cytoplasm connecting many if not all the other cellular organelles (Lev, 2010). Our results show that STARD3 and STARD3NL mediate the formation of LE–ER MCSs through a direct interaction with VAP because of a conserved FFAT-like motif. This supports the notion that discrete molecular bridges exist between similar organelles. These molecular bridges are likely to be differently regulated and participate in distinct cellular functions. Future work should delineate the function of these STARD3- and STARD3NL-mediated MCSs in terms of endosome maturation and lipid traffic.

Materials and Methods

Cloning and constructs

Site-directed mutagenesis was used to generate STARD3 (Q14849-1; natural variant R117Q) and STARD3NL (O95772-1) ΔFFAT mutants (QuikChange, Agilent). The STARD3NL 1–208 mutant was generated by inserting a stop codon in place of residue 209 (Y209X).

HA-hVAP-A and HA-hVAP-B expression plasmids were kind gifts from Dr K. Hanada (NIID, Tokyo, Japan) (Kawano et al., 2006). hVAP-A and hVAP-B were subcloned into pEGFP-C1 vector (Clontech). hVAP-A and hVAP-B were mutated to generate the FFAT-binding-deficient mutants K94D/M96D and K87D/M89D, respectively.

To generate a GFP-ER probe, the coding sequence of *Sac*I C-terminal end [amino acids 521–587; a kind gift from Tamas Balla, NIH, Bethesda, USA (Várnai et al., 2007)] was subcloned into pEGFP-C1.

To obtain shRNA expression vectors targeting VAP-A (target sequence α: 5′-GCGAAATCCATCGGATAGAAA-3′ or β: 5′-CACTTAATGATACCGAAACAA-3′) or VAP-B (α: 5′-GCAGAGAATGATAAACCACAT-3′ or β: 5′-CCAGTTCTGTTTGACTATGTA-3′), oligonucleotides were cloned into the pLKO.1 vector (puromycine or blasticidine resistant) (Moffat et al., 2006).

ON-TARGET plus siRNA pool (Thermo Fisher) transfected with Lipofectamine RNAiMAX reagent (Invitrogen) were used to silence ORP1L (Human-OSBPL1A: 114876) and PTP1B (Human-PTPN1: 5770).

LAMP1 cDNA was obtained from Addgene [plasmid 1816 (Sherer et al., 2003)] and subcloned in fusion with GFP into pQCXIP vector (Clontech).

SDS-PAGE and western blot analysis

SDS-PAGE and western blot analysis were performed as previously described (Alpy et al., 2005) using the following antibodies: STARD3NL: pAbMENTHO-Ct (Alpy

et al., 2002); STARD3: pAbMLN64-Ct-605 (Moog-Lutz et al., 1997); ORP1L: ab131165 (Abcam); PTP1B: 5311 (Cell signaling); VAP-A: K-15 sc-48698 (Santa Cruz biotechnology); VAP-B: rabbit anti-VAP-B (Kabashi et al., 2013); FLAG: F-7425 (Sigma); HA: H-6908 (Sigma); calnexin: C-4731 (Sigma); KDEL: 10C3, sc-58774 (Santa Cruz biotechnology); anti phospho-eIF2α(Ser51) 119A11 (Cell signaling); anti eIF2α 9722 (Cell signaling); actin: ACT-2D7 (Euromedex).

Sequence analysis

STARD3 and STARD3NL sequences from *Homo sapiens*; *Mus musculus*; *Gallus gallus*; *Anolis carolinensis*; *Xenopus siluriana*; *Danio rerio*; *Ciona intestinalis*; *Strongylocentrotus purpuratus*; *Drosophila melanogaster*; *Apis mellifera*; *Daphnia pullex*; *Nematostella vectensis*; *Caenorhabditis elegans*; *Schistosoma mansoni*; *Amphimedon queenslandica* were aligned using ClustalW (Larkin et al., 2007). The consensus sequence was established with EMBOSS (Rice et al., 2000).

Cell culture, transfections and infections

HeLa cells provided by the American Type Culture Collection (Rockville, MD) were maintained in DMEM with 5% fetal calf serum. Cells were transfected using Fugene6 (Roche). For retroviral infection, pQCXIP vectors (pQCXIP STARD3, pQCXIP STARD3NL or empty pQCXIP as control) were co-transfected with pCL-Ampho vector (Imgenex) into BOSC23 retroviral packaging cell line. Retroviral infections were used to generate HeLa/Control, HeLa/STARD3, HeLa/STARD3NL and HeLa/Lamp1-GFP cell lines. Overexpression experiments not using these cell lines were performed by transient transfections.

For lentiviral infection, pLKO.1 vectors were co-transfected with three packaging plasmids pLP1, pLP2 and pLP/VSVG (Invitrogen) into the 293T cell line. Viral particles supplemented with 10 µg/ml polybrene and 20 mM Hepes were then incubated with HeLa cells. Selection was performed using 1 µg/ml puromycin or 1 µg/ml blasticidine.

Immunoprecipitation

Co-immunoprecipitations after cross-linking using Lomant's reagent (UP18971A, Interchim) were performed according to the method of Kumagai et al. (Kumagai et al., 2007). Cell extract fractions were prepared separately to avoid any boiling step.

Electron microscopy

HeLa cells were grown on supports [type-I-collagen-coated aclar film with micro-patterns for correlative light and electron microscopy (CLEM) (Spiegelhalter et al., 2010) or sapphire discs] mounted onto gold-plated live-cell carriers (Leica Microsystems). For CLEM, live-cell images were acquired using a confocal microscope (Leica TCS MP-AOBS, 63×, NA 1.4). Samples were cryoprotected with a solution of 20% BSA in culture medium and immediately frozen at high pressure (EMPACT-2 Leica). Samples were then collected in liquid nitrogen, freeze-substituted and embedded in lowicryl HM20 as previously described (Spiegelhalter et al., 2010). Serial thin sections (60 nm) were cut on an ultramicrotome (Ultracut UCT, Leica Microsystems) and collected on formvar-carbon-coated nickel slot grids. Immunogold labeling was performed on an EM-IGL automate (Leica Microsystems). Rabbit polyclonal anti-GFP (AbCam 6556) was revealed with 10 nm gold-coupled protein A (Utrecht, Netherlands). Sections were stained with uranyl acetate and lead citrate and examined with a transmission electron microscope (Philips CM12). Images were acquired with an Orius 1000 CCD camera (Gatan).

For electron tomography, tilt series (1° steps, from −65 to 65°) from thick sections (200 nm) were collected on a field emission gun electron microscope (Tecnai F20, FEI Company, Eindhoven, The Netherlands) with a Gatan 2K CCD camera. Tomograms were computed (back-projection method) and modeled with the IMOD package (eTomo and 3Dmod modules) (Kremer et al., 1996).

Stereology

A set of virtual horizontal lines separated by 50 nm were randomly placed on TEM images. The perimeter (in nm) of an endosome on the section was estimated using the formula $P=25.\pi.n_i$, (n_i: number of intersections between horizontal lines and the endosome limiting membrane). Similarly, the perimeter of ER–endosome contacts was estimated on the same endosome with the same formula (n_i: number of intersection between horizontal lines and the endosome-limiting membrane in contact with the ER). The proportion of the endosome membrane in contact with the ER was estimated as the ratio between the perimeter of contact over the endosome perimeter. ER–mitochondria contacts were quantified similarly.

Immunofluorescence

Immunofluorescence was performed as previously described (Alpy et al., 2002). Primary antibodies were anti-GFP (GFP-2A3, Euromedex), anti-FLAG (F-7425 Sigma) and for endogenous staining anti-VAP-A (K-15 – Santa Cruz Biotechnology, sc-48698) and pAbMENTHO-Ct (Alpy et al., 2002). Slides were mounted in ProLong Gold (Invitrogen). Observations were made with a confocal microscope (Leica SP2 UV, 63×, NA 1.4). Linescans were drawn using ImageJ software (plot profile function; http://rsbweb.nih.gov/ij/). Pearson's correlation coefficients were calculated with Excel. Colocalization was visualized using the colocalization highlighter plug-in for ImageJ.

In situ proximity ligation assay

The proximity ligation assay was performed with the Duolink system (Olink bioscience). After fixation in ethanol and acetone, endogenous STARD3, STARD3NL and VAP-A were detected using pAbMLN64-Nt (Alpy et al., 2001), pAbMENTHO-Ct and anti-VAP-A K-15, respectively. PLA dots were acquired with a spinning disk confocal microscope (Andor Revolution). Quantifications were performed with ICY software (spot detector function; http://icy.bioimageanalysis.org). LAMP1 labeling (mouse anti-LAMP1; Developmental Studies Hybridoma Bank; H4A3) was performed after PLA staining.

FRET-FLIM

HeLa cells grown in Phenol-Red-free medium on 35 mm glass-bottomed dishes (MatTek) were co-transfected with expression plasmids encoding a FRET pair (EGFP/mCherry). FLIM was performed using an inverted laser scanning multiphoton microscope (Leica SP2 AOBS MP) with a HCX-PAN-APO-63× 1.4 NA objective. The microscope was in a black chamber at 37°C (Life Imaging Services, Cube&Box) for living sample observations. Two-photon excitation of EGFP was achieved using a femtosecond (repetition frequency of 80 MHz) Tsunami laser (Spectra Physics) set at 904 nm. The fluorescence lifetime was measured using the time correlated single photon counting (TCSPC) approach with a SPC 830 photon counting card (Becker & Hickl GmbH). A single photon detector (PMC 100; Becker & Hickl) was located after a stop filter (515/30 nm; Chroma Technology) in order to record photons coming from the donor only. The laser power was adjusted to give a mean photon count rate of 10^4–10^5 photons/second. Each sample was scanned for 180 seconds to achieve sufficient measurements for statistical analysis. The mean fluorescence lifetime was calculated for pixels within a 256×256 pixels field corresponding to a 59 µm×59 µm area using SPCImage software (Becker & Hickl). A monoexponential fluorescence decay model was applied to fit the experimental fluorescence decay curves.

Time-lapse microscopy

Live cells were placed in a thermostatic chamber (37°C, 5% CO_2; Tokai) mounted on a Leica DMI6000 microscope (Leica Microsystems). Images were acquired by an EM-CCD camera (Andor iXon; Andor Technology) coupled to a Yokogawa spinning-disc confocal unit CSU22 (Yokogawa Electric Corp). To measure tubule to vesicle index, a stereological method was used (Mayhew, 1991). A set of virtual horizontal lines separated by 1.2 µm were randomly placed on images. Tubule to vesicle index was evaluated by dividing the number of intersections between horizontal lines and tubules by the number intersections between horizontal lines and GFP-positive structures (tubules+vesicles). Three measurements (time points 00:20, 1:00, 1:40; minutes:seconds) were averaged per time-lapse sequence.

Statistical analyses

Unless otherwise specified, statistical analyses were performed using Student's *t*-test. The Mann–Whitney test was used for stereology results (VassarStats http://vassarstats.net/). *P*-values of <0.05, <0.01 and <0.001 are identified with 1, 2 and 3 asterisks, respectively.

Acknowledgements

We thank Dr Kentaro Hanada for providing HA-VAPA and HA-VAPB expression plasmids as well as valuable advice; Tamas Balla for providing the Sac1 expression vector; Luc Dupuis for providing the anti-VAP-B antibody. We thank Françoise Hullin-Matsuda, Toshihide Kobayashi, Guillaume Drin, Bruno Mesmin, Karim Hnia, Shankar Pattabhiraman and the members of the Molecular and Cellular Biology of Breast Cancer team (IGBMC) for helpful advice and discussions. We thank Marc Koch and Claire Pieraerts for their excellent technical assistance; Patrick Schultz, Danièle Spehner and Corinne Crucifix for access to the HPF apparatus and TEM for EM tomography.

Author contributions

F.A., T.P.L. and C.T. conceived and designed the study; F.A., A.R., Y.S., F.L., I.S., C.W., C.S., P.K. designed and performed the experiments; F.A., A.R., Y.S., P.K., C.M., M.C.R. analyzed the data; F.A., T.P.L. and C.T. wrote the paper.

Funding

This work was funded by the Ministère de l'Enseignement Supérieur et de la Recherche [fellowship to A.R.]; the Japan Society for the

Promotion of Science/University of Strasbourg [travel grant to F.A.]; Alsace contre le cancer [fellowship to F.L.]; the Institut National de Santé et de Recherche Médicale; the Centre National de la Recherche Scientifique; the Université de Strasbourg; and the Ligue Nationale Contre le Cancer (Programme Labelisation).

Supplementary material available online at
http://jcs.biologists.org/lookup/suppl/doi:10.1242/jcs.139295/-/DC1

References

Alpy, F. and Tomasetto, C. (2005). Give lipids a START: the StAR-related lipid transfer (START) domain in mammals. *J. Cell Sci.* **118**, 2791-2801.

Alpy, F. and Tomasetto, C. (2006). MLN64 and MENTHO, two mediators of endosomal cholesterol transport. *Biochem. Soc. Trans.* **34**, 343-345.

Alpy, F., Stoeckel, M. E., Dierich, A., Escola, J. M., Wendling, C., Chenard, M. P., Vanier, M. T., Gruenberg, J., Tomasetto, C. and Rio, M. C. (2001). The steroidogenic acute regulatory protein homolog MLN64, a late endosomal cholesterol-binding protein. *J. Biol. Chem.* **276**, 4261-4269.

Alpy, F., Wendling, C., Rio, M. C. and Tomasetto, C. (2002). MENTHO, a MLN64 homologue devoid of the START domain. *J. Biol. Chem.* **277**, 50780-50787.

Alpy, F., Latchumanan, V. K., Kedinger, V., Janoshazi, A., Thiele, C., Wendling, C., Rio, M. C. and Tomasetto, C. (2005). Functional characterization of the MENTAL domain. *J. Biol. Chem.* **280**, 17945-17952.

de Brito, O. M. and Scorrano, L. (2008). Mitofusin 2 tethers endoplasmic reticulum to mitochondria. *Nature* **456**, 605-610.

De Vos, K. J., Mórotz, G. M., Stoica, R., Tudor, E. L., Lau, K. F., Ackerley, S., Warley, A., Shaw, C. E. and Miller, C. C. (2012). VAPB interacts with the mitochondrial protein PTPIP51 to regulate calcium homeostasis. *Hum. Mol. Genet.* **21**, 1299-1311.

Dion, P. A., Dupre, N. and Hollinger, D. et al. (2013). Investigating the contribution of VAPB/ALS8 loss of function in amyotrophic lateral sclerosis. *Hum. Mol. Genet.* **22**, 2350-2360.

Eden, E. R., White, I. J., Tsapara, A. and Futter, C. E. (2010). Membrane contacts between endosomes and ER provide sites for PTP1B-epidermal growth factor receptor interaction. *Nat. Cell Biol.* **12**, 267-272.

Elbaz, Y. and Schuldiner, M. (2011). Staying in touch: the molecular era of organelle contact sites. *Trends Biochem. Sci.* **36**, 616-623.

Friedman, J. R., Dibenedetto, J. R., West, M., Rowland, A. A. and Voeltz, G. K. (2013). Endoplasmic reticulum-endosome contact increases as endosomes traffic and mature. *Mol. Biol. Cell* **24**, 1030-1040.

Hanada, K., Kumagai, K., Yasuda, S., Miura, Y., Kawano, M., Fukasawa, M. and Nishijima, M. (2003). Molecular machinery for non-vesicular trafficking of ceramide. *Nature* **426**, 803-809.

Hanada, K., Kumagai, K., Tomishige, N. and Yamaji, T. (2009). CERT-mediated trafficking of ceramide. *Biochim. Biophys. Acta* **1791**, 684-691.

Helle, S. C. J., Kanfer, G., Kolar, K., Lang, A., Michel, A. H. and Kornmann, B. (2013). Organization and function of membrane contact sites. *Biochim. Biophys. Acta* **1833**, 2526-2541.

Hölttä-Vuori, M., Alpy, F., Tanhuanpää, K., Jokitalo, E., Mutka, A. L. and Ikonen, E. (2005). MLN64 is involved in actin-mediated dynamics of late endocytic organelles. *Mol. Biol. Cell* **16**, 3873-3886.

Kaiser, S. E., Brickner, J. H., Reilein, A. R., Fenn, T. D., Walter, P. and Brunger, A. T. (2005). Structural basis of FFAT motif-mediated ER targeting. *Structure* **13**, 1035-1045.

Kawano, M., Kumagai, K., Nishijima, M. and Hanada, K. (2006). Efficient trafficking of ceramide from the endoplasmic reticulum to the Golgi apparatus requires a VAMP-associated protein-interacting FFAT motif of CERT. *J. Biol. Chem.* **281**, 30279-30288.

Kremer, J. R., Mastronarde, D. N. and McIntosh, J. R. (1996). Computer visualization of three-dimensional image data using IMOD. *J. Struct. Biol.* **116**, 71-76.

Kumagai, K., Kawano, M., Shinkai-Ouchi, F., Nishijima, M. and Hanada, K. (2007). Interorganelle trafficking of ceramide is regulated by phosphorylation-dependent cooperativity between the PH and START domains of CERT. *J. Biol. Chem.* **282**, 17758-17766.

Larkin, M. A., Blackshields, G., Brown, N. P., Chenna, R., McGettigan, P. A., McWilliam, H., Valentin, F., Wallace, I. M., Wilm, A., Lopez, R. et al. (2007). Clustal W and Clustal X version 2.0. *Bioinformatics* **23**, 2947-2948.

Lev, S. (2010). Non-vesicular lipid transport by lipid-transfer proteins and beyond. *Nat. Rev. Mol. Cell Biol.* **11**, 739-750.

Lev, S., Ben Halevy, D., Peretti, D. and Dahan, N. (2008). The VAP protein family: from cellular functions to motor neuron disease. *Trends Cell Biol.* **18**, 282-290.

Levine, T. and Loewen, C. (2006). Inter-organelle membrane contact sites: through a glass, darkly. *Curr. Opin. Cell Biol.* **18**, 371-378.

Liapis, A., Chen, F. W., Davies, J. P., Wang, R. and Ioannou, Y. A. (2012). MLN64 transport to the late endosome is regulated by binding to 14-3-3 via a non-canonical binding site. *PLoS ONE* **7**, e34424.

Llères, D., James, J., Swift, S., Norman, D. G. and Lamond, A. I. (2009). Quantitative analysis of chromatin compaction in living cells using FLIM-FRET. *J. Cell Biol.* **187**, 481-496.

Loewen, C. J. and Levine, T. P. (2005). A highly conserved binding site in vesicle-associated membrane protein-associated protein (VAP) for the FFAT motif of lipid-binding proteins. *J. Biol. Chem.* **280**, 14097-14104.

Loewen, C. J., Roy, A. and Levine, T. P. (2003). A conserved ER targeting motif in three families of lipid binding proteins and in Opi1p binds VAP. *EMBO J.* **22**, 2025-2035.

Manford, A. G., Stefan, C. J., Yuan, H. L., Macgurn, J. A. and Emr, S. D. (2012). ER-to-plasma membrane tethering proteins regulate cell signaling and ER morphology. *Dev. Cell* **23**, 1129-1140.

Mayhew, T. M. (1991). The new stereological methods for interpreting functional morphology from slices of cells and organs. *Exp. Physiol.* **76**, 639-665.

Mikitova, V. and Levine, T. P. (2012). Analysis of the key elements of FFAT-like motifs identifies new proteins that potentially bind VAP on the ER, including two AKAPs and FAPP2. *PLoS ONE* **7**, e30455.

Moffat, J., Grueneberg, D. A., Yang, X., Kim, S. Y., Kloepfer, A. M., Hinkle, G., Piqani, B., Eisenhaure, T. M., Luo, B., Grenier, J. K. et al. (2006). A lentiviral RNAi library for human and mouse genes applied to an arrayed viral high-content screen. *Cell* **124**, 1283-1298.

Moog-Lutz, C., Tomasetto, C., Régnier, C. H., Wendling, C., Lutz, Y., Muller, D., Chenard, M. P., Basset, P. and Rio, M. C. (1997). MLN64 exhibits homology with the steroidogenic acute regulatory protein (STAR) and is over-expressed in human breast carcinomas. *Int. J. Cancer* **71**, 183-191.

Nishimura, Y., Hayashi, M., Inada, H. and Tanaka, T. (1999). Molecular cloning and characterization of mammalian homologues of vesicle-associated membrane protein-associated (VAMP-associated) proteins. *Biochem. Biophys. Res. Commun.* **254**, 21-26.

Pfeffer, S. (2003). Membrane domains in the secretory and endocytic pathways. *Cell* **112**, 507-517.

Ponting, C. P. and Aravind, L. (1999). START: a lipid-binding domain in StAR, HD-ZIP and signalling proteins. *Trends Biochem. Sci.* **24**, 130-132.

Rice, P., Longden, I. and Bleasby, A. (2000). EMBOSS: the European Molecular Biology Open Software Suite. *Trends Genet.* **16**, 276-277.

Rocha, N., Kuijl, C., van der Kant, R., Janssen, L., Houben, D., Janssen, H., Zwart, W. and Neefjes, J. (2009). Cholesterol sensor ORP1L contacts the ER protein VAP to control Rab7-RILP-p150 Glued and late endosome positioning. *J. Cell Biol.* **185**, 1209-1225.

Russell, M. R., Nickerson, D. P. and Odorizzi, G. (2006). Molecular mechanisms of late endosome morphology, identity and sorting. *Curr. Opin. Cell Biol.* **18**, 422-428.

Sachse, M., Ramm, G., Strous, G. and Klumperman, J. (2002). Endosomes: multipurpose designs for integrating housekeeping and specialized tasks. *Histochem. Cell Biol.* **117**, 91-104.

Sherer, N. M., Lehmann, M. J., Jimenez-Soto, L. F., Ingmundson, A., Horner, S. M., Cicchetti, G., Allen, P. G., Pypaert, M., Cunningham, J. M. and Mothes, W. (2003). Visualization of retroviral replication in living cells reveals budding into multivesicular bodies. *Traffic* **4**, 785-801.

Skehel, P. A., Fabian-Fine, R. and Kandel, E. R. (2000). Mouse VAP33 is associated with the endoplasmic reticulum and microtubules. *Proc. Natl. Acad. Sci. USA* **97**, 1101-1106.

Söderberg, O., Gullberg, M., Jarvius, M., Ridderstråle, K., Leuchowius, K. J., Jarvius, J., Wester, K., Hydbring, P., Bahram, F., Larsson, L. G. et al. (2006). Direct observation of individual endogenous protein complexes in situ by proximity ligation. *Nat. Methods* **3**, 995-1000.

Spiegelhalter, C., Tosch, V., Hentsch, D., Koch, M., Kessler, P., Schwab, Y. and Laporte, J. (2010). From dynamic live cell imaging to 3D ultrastructure: novel integrated methods for high pressure freezing and correlative light-electron microscopy. *PLoS ONE* **5**, e9014.

Toulmay, A. and Prinz, W. A. (2011). Lipid transfer and signaling at organelle contact sites: the tip of the iceberg. *Curr. Opin. Cell Biol.* **23**, 458-463.

Trowbridge, I. S., Collawn, J. F. and Hopkins, C. R. (1993). Signal-dependent membrane protein trafficking in the endocytic pathway. *Annu. Rev. Cell Biol.* **9**, 129-161.

Tsujishita, Y. and Hurley, J. H. (2000). Structure and lipid transport mechanism of a StAR-related domain. *Nat Struct Mol Biol.* **7**, 408-414.

van der Kant, R., Zondervan, I., Janssen, L. and Neefjes, J. (2013). Cholesterol-binding molecules MLN64 and ORP1L mark distinct late endosomes with transporters ABCA3 and NPC1. *J. Lipid Res.* **54**, 2153-2165.

van Weering, J. R., Verkade, P. and Cullen, P. J. (2012). SNX-BAR-mediated endosome tubulation is co-ordinated with endosome maturation. *Traffic* **13**, 94-107.

Várnai, P., Tóth, B., Tóth, D. J., Hunyady, L. and Balla, T. (2007). Visualization and manipulation of plasma membrane-endoplasmic reticulum contact sites indicates the presence of additional molecular components within the STIM1-Orai1 Complex. *J. Biol. Chem.* **282**, 29678-29690.

Zhang, M., Liu, P., Dwyer, N. K., Christenson, L. K., Fujimoto, T., Martinez, F., Comly, M., Hanover, J. A., Blanchette-Mackie, E. J. and Strauss, J. F., III (2002). MLN64 mediates mobilization of lysosomal cholesterol to steroidogenic mitochondria. *J. Biol. Chem.* **277**, 33300-33310.